

Non-maximal entanglement of photons from positron-electron annihilation demonstrated using a novel plastic PET scanner

P. Moskal^{1,2,3,*}, D. Kumar^{1,2,3}, S. Sharma^{1,2,3,**}, E.Y. Beyene^{1,2,3}, N. Chug^{1,2,3}, A. Coussat^{1,2,3},
C. Curceanu⁴, E. Czerwiński^{1,2,3}, M. Das^{1,2,3}, K. Dulski^{1,2,3}, M. Gorgol⁵, B. Jasińska⁵,
K. Kacprzak^{1,2,3}, T. Kaplanoglu^{1,2,3}, Ł. Kapłon^{1,2,3}, K. Klimaszewski⁶, T. Kozik^{1,2,3},
E. Lisowski⁸, F. Lisowski⁸, W. Mryka^{1,2,3}, S. Niedźwiecki^{1,2,3}, S. Parzych^{1,2,3}, E.P. del Rio^{1,2,3},
L. Raczyński⁶, M. Rädler^{1,2,3}, R.Y. Shopa⁶, M. Skurzok^{1,2,3}, E. Ł. Stępień^{1,2,3}, P. Tanty^{1,2,3},
K. Tayefi Ardebili^{1,2,3}, K. Valsan Eliyan^{1,2,3}, and W. Wiślicki⁶

¹Faculty of Physics, Astronomy and Applied Computer Science, Jagiellonian University,
S. Łojasiewicza 11, 30-348 Kraków, Poland

²Total-Body Jagiellonian-PET Laboratory, Jagiellonian University, Poland

³Center for Theranostics, Jagiellonian University, 31-034 Kraków, Poland

⁴INFN, Laboratori Nazionali di Frascati CP 13, Via E. Fermi 40, 00044, Frascati, Italy

⁵Institute of Physics, Maria Curie-Skłodowska University, Pl. M. Curie-Skłodowskiej 1, 20-031
Lublin, Poland

⁶Department of Complex Systems, National Centre for Nuclear Research, 05-400
Otwock-Świerk, Poland

⁷Institute of Applied Computer Science, Jagiellonian University, Kraków, Poland

⁸Cracow University of Technology, 31-864 Kraków, Poland

*corresponding author, e-mail: p.moskal@uj.edu.pl

**corresponding author, e-mail: sushil.sharma@uj.edu.pl

Abstract

In the state-of-the-art Positron Emission Tomography (PET), information about polarization of annihilation photons is not available. Current PET systems track molecules labeled with positron-emitting radioisotopes by detecting the propagation direction of two photons originating from positron-electron annihilation. However, annihilation photons carry more information than just about the site where they originated. Here we present a novel J-PET scanner built from plastic scintillators in which annihilation photons interact predominantly via Compton effect, thus providing information about photons' polarization in addition to information of photons' direction of propagation. Theoretically, photons from the decay of positronium in vacuum are maximally entangled in polarization. However, in matter when the positron from positronium annihilates with the electron bound to the atom, the question naturally arises as to whether the photons resulting from such annihilation are maximally entangled. In this work, using the J-PET scanner, we determine the distribution of the relative angle between polarization orientations of two photons from

positron-electron annihilation in a porous polymer. Contrary to previous results for positron annihilation in aluminum and copper, where the strength of observed correlation is as expected for maximally entangled photons, our results show a significant deviation from this behavior. We demonstrate that in porous polymer the correlation between the photons polarization is weaker than predicted for the maximally quantum-entangled two-photon state, but stronger than expected for separable photons. The data indicate that more than 40% of annihilations in Amberlite resin is leading to non-maximally entangled state.

Our result indicates the dependence of the degree of correlation on the annihilation mechanism and hence on the molecular arrangement. We anticipate that the introduced Compton interaction based PET system opens a promising perspective for the exploration of polarization correlations in PET as a novel diagnostic indicator.

INTRODUCTION

Positron emission tomography (PET) is an established imaging technique for noninvasive *in vivo* diagnosis of disease in clinical practice [1–4]. Its potential for quantitative assessment of metabolic alteration in biological tissues makes it useful for various medical applications by assessing physiology (functionality) of human organs or tissues [1, 5]. In PET a biomolecular tracer labeled with a positron (e^+) emitting radionuclide is administered into the human body. The emitted e^+ interacts with electron (e^-) in the tissue and annihilates predominantly into two 511 keV photons moving in opposite directions. The principle of PET is based on the registration of places and times of interactions of these two photons, and reconstruction of the site of annihilation along their direction of propagation referred to as Line of Response (LOR). The information from the LORs is used as input to reconstruct the density distribution of annihilation points. However, annihilation photons carry more information than just about the site where they originated. Generally, annihilation photons carry information in the form of energy, direction of propagation, polarization, and the degree of entanglement [6–8]. Polarization of annihilation photons is not accessible by current PET systems, but in principle it can inform us about the contributing annihilation mechanisms, that in turn may tell us about the cell molecular composition. In the body (Fig. 1(a)), a positron emitted from the isotope attached to the biomolecule may annihilate with an electron either directly or via formation of positronium [9, 10]. Positronium in the tissue intermediates the positron-electron annihilation in about 40% of cases [11–13]. Positronium may be formed as a long lived (142 ns) spin-one ortho-positronium (oPs), or as a short lived (125 ps) spin-zero parapositronium (pPs) [14]. In vacuum oPs decays into 3-photons ($\text{oPs} \rightarrow 3\gamma$) and pPs into 2-photons ($\text{pPs} \rightarrow 2\gamma$) [10]. Theoretically, photons from the decay of positronium in vacuum are maximally entangled in polarization [15–17]. However, in matter when positron from positronium annihilates with the electron bound to the atom, it is natural to ask the question of whether the photons resulting from such annihilation are maximally entangled

[18–21].

Annihilation photons possess energy in the range of MeV and hence interact in matter with single electrons. Therefore, their polarization cannot be studied using optical methods. However, polarization of

such high energetic photons can be estimated by Compton scattering (Fig. 1b). The Compton scattering of photons is most likely in a plane perpendicular to the polarization of the incoming photon [22], and therefore polarization orientation of the primary photon ($\vec{\varepsilon}$) at the moment of scattering can approximately be determined as a vector product of momentum vectors of initial \vec{k} and scattered photon \vec{k}' [23].

$$\vec{\varepsilon} = \frac{\vec{k} \times \vec{k}'}{|\vec{k}_i \times \vec{k}'_i|} \quad (1)$$

Fig. 1(c) describes the distribution of η [24], the relative angle between polarization plane and scattering plane, as a function of the scattering angle θ . It indicates that, in case of 511 keV annihilation photons, the correlation between the polarization direction $\vec{\varepsilon}$ and the scattering plane is maximal at about $\theta = 82^\circ$ decreasing to negligible effect for forward ($\theta = 0^\circ$) and backward ($\theta = 180^\circ$) scattering. In general the analysing power (A_p) of the Compton polarimeter is expressed as [16, 25, 26]:

$$A_p = \sin^2\theta / (E/E' + E'/E - \sin^2\theta), \quad (2)$$

where E and E' denotes the energy of primary and scattered photon, respectively [26]. For 511 keV photons, maximum value of A_p equal to 0.69 is reached at $\theta = 82^\circ$. The distribution shown in Fig. 1(c) indicates that the Compton scattering may be effectively applied as polarimeter in the scattering angle range of about $\theta = 82^\circ \pm 30^\circ$, in which analysing power varies from 0.69 to 0.42. This range is indicated by horizontal dashed lines. For the 2γ annihilation process (Fig. 1(d)), when each γ interacts via Compton scattering with an electron, one can estimate the relative angle between the polarization directions of the photons $|\eta_1 - \eta_2|$ by measurement of the relative angle $\Delta\varphi$ between the scattering planes [24]. Bose-symmetry and parity conservation in the decay of para-positronium (pPs) imply that the state $|\psi\rangle$ of the resulting two photons is maximally entangled and that the photons polarizations are orthogonal to each other [16]. In the linear polarization base the 2-photon state from pPs decay reads:

$$|\psi\rangle = \frac{1}{\sqrt{2}}(|H\rangle_1|V\rangle_2 - |V\rangle_1|H\rangle_2), \quad (3)$$

where H and V correspond to the horizontal and vertical polarization directions. Taking into account the Compton scattering of each of the photons, the double Compton scattering differential cross section can be expressed as [27]:

$$\frac{d^2\sigma(\theta_1, \theta_2, \Delta\varphi)}{d\Omega_1 d\Omega_2} = [A(\theta_1, \theta_2) - B(\theta_1, \theta_2)\cos(2(\Delta\varphi))], \quad (4)$$

where, A and B describe dependence of the cross section on the Compton scattering angles θ_1 and θ_2 . At given scattering angles (θ_1, θ_2) , the cross section is maximal for $\Delta\varphi = 90^\circ$ and minimum for $\Delta\varphi = 0^\circ$. The strength of the polarization correlation of the annihilation photons may be described by R factor (referred to as entanglement witness), which is the ratio of the probabilities of the scattering at $\Delta\varphi = 90^\circ$

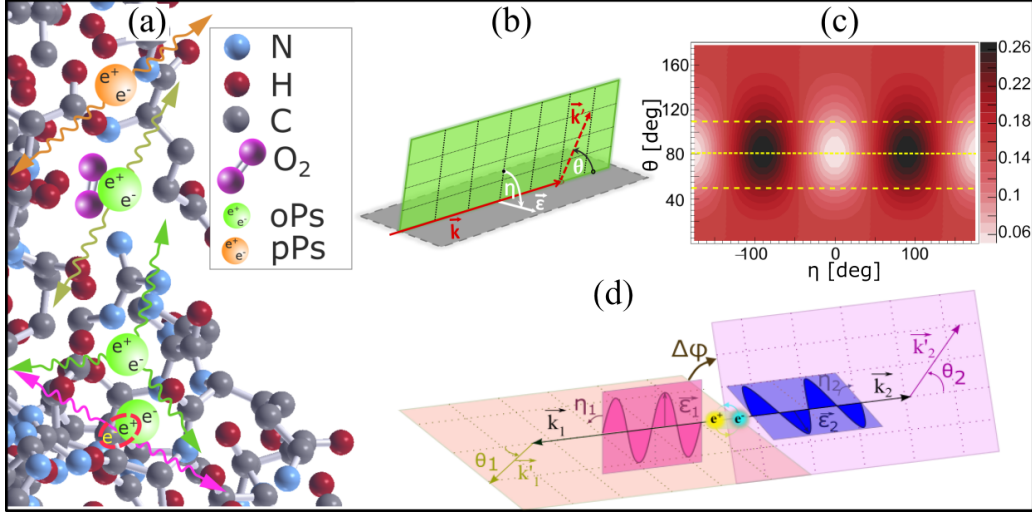


Fig. 1. **(a)** Pictorial illustration of positronium annihilations in the intramolecular cavities of the hemoglobine molecule. Parapositronium (pPs, orange) decays into two counter-propagating 511 keV photons. Orthopositronium (oPs, green) self-annihilates into three photons (green arrows), but can also decay into two photons (violet arrows) when the positron picks off an electron from the atom (indicated by red ellipse), or when oPs converts to pPs via interaction with paramagnetic oxygen molecule (indicated as two violet circles). **(b)** Pictorial illustration of the photon-electron Compton scattering with the definition of the photon scattering angle (θ), photon polarization ($\vec{\epsilon}$), photon momentum before (\vec{k}) and after (\vec{k}') the scattering, and the angle (η) between the polarization and scattering planes. **(c)** Normalized Klein-Nishina cross section for 511 keV photons as a function of angles η (horizontal axis) and θ (vertical axis). For normalization, the 2D plot (η , θ) was weighted such that for each value of θ the integral of cross-section over the entire range of η from $-\pi$ to π is equal to unity. The yellow dotted line indicates the value of $\theta = 82^\circ$, for which visibility is maximum [16] and dashed lines indicate a range of high visibility for $\theta = 82^\circ \pm 30^\circ$ [24]. **(d)** Schematic representation of annihilation photons and their Compton scattering, including polarization and scattering planes. θ_1 and θ_2 denote the Compton scattering angles. η_1 and η_2 denote angles between the scattering and polarization planes. $\Delta\varphi$ represents the angle between the scattering planes of annihilation photons and thus is a measure of the relative angle between their polarization planes.

and $\Delta\varphi = 0^\circ$. This implies:

$$R = \frac{A(\theta_1, \theta_2) + B(\theta_1, \theta_2)}{A(\theta_1, \theta_2) - B(\theta_1, \theta_2)}, \quad (5)$$

The maximum of the cross section at $\Delta\varphi = 90^\circ$ reflects the fact that the polarizations of the photons are perpendicular to each other. For maximally entangled photons, the value of R reaches a maximum of 2.84 at the scattering angles of $\theta_1 = \theta_2 = 82^\circ$ [16, 27–35], while for separable photons the maximum value of R is equal to 1.63 [33, 34]. The shape of the distribution of the angle $\Delta\varphi$ can in principle carry information about the molecular composition of annihilation sites. In matter, 2γ annihilations (used in PET) occur either by (i) direct electron-positron annihilation, (ii) via self-annihilation of pPs or (iii) via oPs annihilation due to interaction with surrounding electrons (Fig. 1(a)). The oPs in addition to self-annihilation into 3-photons, may annihilate into 2-photons when the positron from ortho-positronium picks off electron from the surrounding molecular environment (pick-off process) [10]. Here we hypothesize that the $\Delta\varphi$ distribution may depend on the annihilation mechanism. This would mean that value of R depends on the material and may serve as an indicator of the intra-molecular environment surrounding

the positronium. In this work we present a dedicated positron emission tomography scanner, called the Jagiellonian PET (J-PET), build from plastic scintillators in which annihilation photons interact solely via Compton scattering (with photoelectric effect at the level of 10^{-5} [36]). In the J-PET scanner, the average distance between the primary and secondary scattering of 511 keV photon is equal to about 25 cm (compared to about 0.6 cm in crystal PET systems) rendering possible measurement of the $\Delta\varphi$ distribution with high angular resolution [24]. We substantiate the capability of the J-PET scanner in effectively imaging the $\Delta\varphi$ distribution and hence for imaging of parameter R in addition to the standard PET imaging of the density distribution of annihilation points. As an example of application we determine that value of R for photons from the positron-electron annihilation in porous polymer is significantly lower than expected for maximally entangled photons, and by comparison to the value of R determined for aluminum, we demonstrate that R is sensitive to the type of the material. This result opens up prospects for using entanglement witness R as a diagnostic parameter of tissue type and tissue pathology. Finally, we estimate and discuss the sensitivity of the total-body J-PET scanner for the simultaneous PET and R value imaging in clinical diagnostics.

RESULTS

This work experimentally demonstrates for the first time the dependence of the degree of entanglement of annihilation photons on the type of the material in which the positron annihilates, and presents the capability of newly developed J-PET scanner to image the quantum correlation of annihilation photons. Figs. 2a and 2b show photographs of the J-PET scanner developed and constructed by the J-PET group [36–43]. The technical details of the J-PET scanner and the annihilation chamber are outlined in the Methods section. In this section, we highlight the key features that set J-PET apart from the current PET scanners and make it capable of imaging quantum entanglement of annihilation photons. The J-PET scanner is built from plastic scintillator strips arranged axially with the photomultiplier readout at the ends. Application of plastic scintillators, instead of crystals used in the state-of-the-art PET systems, and the application of dedicated triggerless data acquisition system are the two crucial novelties enabling efficient detection of events in which both photons from $e^+e^- \rightarrow 2\gamma$ annihilation undergoes Compton scattering. In plastic scintillators 511 keV annihilation photons interact via Compton scattering only (fraction of photoelectric effect is at the order of 10^{-5} [36]), and triggerless acquisition enables simultaneous detection of 4 interactions due to annihilation and scattered photons. Contrary to the state-of-the-art PET systems in which signal processing and acquisition are confined to two interactions only [2, 44, 45]. The registration of Compton scattered photons is mandatory for the determination of the annihilation photon's polarization. The linear polarization of the i^{th} annihilation photon is determined using equation 1 [23, 24].

A typical topology of events used in this study is superimposed on the photograph of the scanner (Fig. 2a), and on its schematic cross section (Fig. 2c). Positron-electron annihilation occurs in the porous polymer XAD4 [46] surrounding the positron emitting ^{22}Na source placed in annihilation chamber Fig.2b.

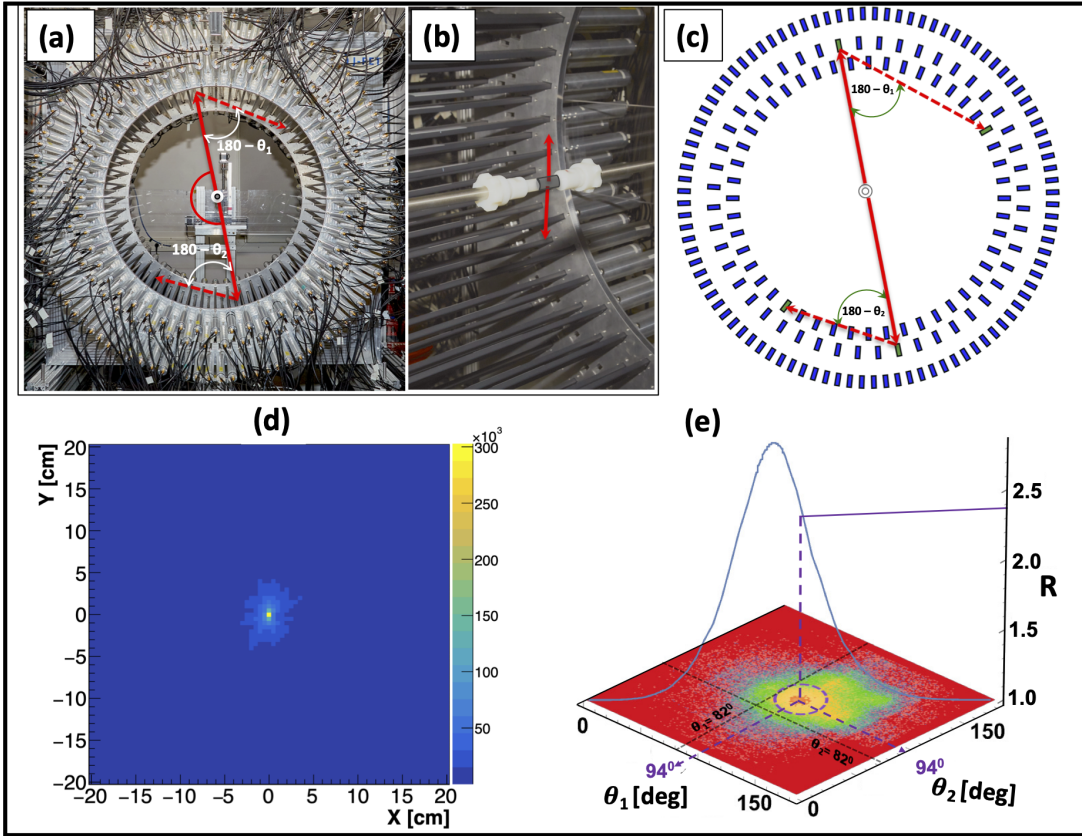


Fig. 2. (a) Photograph of the 192 strip J-PET tomograph with superimposed illustration of the example event with annihilation photons (solid red arrows) and scattered photons (dashed red arrows) used in this study. (b) Close-up photograph of the annihilation chamber, which comprises a positron emitting ^{22}Na radionuclide surrounded by XAD4 porous polymer [46]. In this photograph, scintillator strips covered with black light-tight foil and aluminum photomultiplier housings are visible. (c) The cross-section of the 192 strip J-PET scanner together with the annihilation photons (solid red lines) originating from the electron-positron annihilation in the chamber, and the scattered photons (dashed red lines). (d) Tomographic image of the annihilation source with a pixel size of $5 \text{ mm} \times 5 \text{ mm}$. (e) Experimentally determined distribution of scattering angles θ_2 vs. θ_1 . The maximum density of events determined at $\theta_1 = \theta_2 = 94^\circ$ is due to the geometry of the detector, as can be seen in Figs. (a) and (b). The superimposed solid-blue curve indicates the value of entanglement witness R calculated for the cases where $\theta_1 = \theta_2$. The maximum of $R = 2.84$ is visible for $\theta_1 = \theta_2 = 82^\circ$, while the experimental data concentrates around $\theta_1 = \theta_2 = 94^\circ$ where $R = 2.4$.

The two annihilation photons are emitted in opposite directions and registered in the three-layer J-PET system consisting of 192 plastic scintillators of 50 cm length and a cross section of $1.9 \times 0.7 \text{ cm}^2$ [40]. The signals from photomultipliers are sampled by dedicated electronics [47] enabling determination of time, position and energy deposition for each registered photon interaction [40]. Interactions are referred to as hits. For an event of interest, four hits are required, two hits from annihilation photons and two hits from scattered photons. Hits in the detector caused by the annihilation photons are distinguished from hits due to scattered photons based on the registered energy deposition and angular correlations. Hits from

annihilation photons are used to reconstruct the tomographic image of the annihilation source. An example image, showing the reconstructed position of the source, is presented in Fig. 2(d). Next, each scattered photon is assigned to the appropriate annihilation photon using information on time and positions of hits. The events selection criteria are discussed in detail in the Methods section. Once the hits in the event are identified, the scatterings angles (θ_1 and θ_2) and the angle between the scattering planes ($\Delta\varphi$) are determined. The determined distribution of the θ_1 versus θ_2 angles is shown in Fig. 2e. It illustrates that the maximum of the density distribution of registered events is around the angles of $\theta_1 = \theta_2 = 94^\circ$. This is due to the geometric arrangements of scintillators in the J-PET tomograph, as can be seen in Fig. 2c. Solid curve superimposed on the plot in Fig. 2e indicate the distribution of entanglement witness R for scatterings where $\theta_1 = \theta_2$, calculated under the assumption that the annihilation photons are maximally entangled. It shows that the value of R expected at maximum of the density distribution of registered events is equal to $R = 2.4$, and it is lower than that the maximal value of $R = 2.84$ for $\theta_1 = \theta_2 \approx 82^\circ$. For further analysis of the experimental data, we selected the region around $\theta_1 = \theta_2 = 82^\circ$, where the highest correlation is expected, and the region around $\theta_1 = \theta_2 = 94^\circ$, where the highest number of events is recorded. Fig. 3a and Fig. 3b show the $\Delta\varphi$ distribution determined for events with the θ_1, θ_2 scattering angles from the circle of radius $r = 20^\circ$ centered at $\theta_1 = \theta_2 = 82^\circ$ (Fig. 3a) and at $\theta_1 = \theta_2 = 94^\circ$ (Fig. 3b), respectively. The studied regions on the (θ_1, θ_2) plot are shown in the Methods section. The formula $A - B \cos(2\Delta\varphi)$ was fitted to the determined distributions in order to extract the value of $R_{exp} = (A + B)/(A - B)$. The blue curves depict the results of the fits superimposed on the data, and the resultant values of R_{exp} are represented by blue circles in Fig. 3c and Fig. 3d. The experimental values of R_{exp} that were obtained correspond to the weighted average of R values, where the weights are based on the density distribution of registered events over the selected region on the (θ_1, θ_2) distribution. In the figure, the experimental results are compared to the theoretical predictions obtained under two assumptions: (i) that the photons are maximally entangled (green triangles pointing upwards) and (ii) that the photons are in a separable state (magenta triangles pointing downwards). The shown theoretical predictions account for the effects of the detection system, which were modeled using Monte Carlo simulation methods as described in detail in the Methods section. The measured experimental values of the entanglement witness R_{exp} (given in Table I) are smaller than the predicted values for maximally entangled photons R_{sim}^{max} , and larger than the expected values for separable photons R_{sim}^{sep} . The difference between the experimental and theoretical values of the entanglement witness R remains consistent across all studied regions with radius r ranging from $r = 10^\circ$ to $r = 30^\circ$. As the radius increases, the experimental value of R_{exp} decreases, and the statistical errors also decrease. For the mean radius of $r = 20^\circ$, the determined values of R_{exp} for the distribution of scattering angles centered at $\theta_1 = \theta_2 = 82^\circ$ and $\theta_1 = \theta_2 = 94^\circ$ are estimated to be 2.00 ± 0.03 and 1.93 ± 0.03 , respectively.

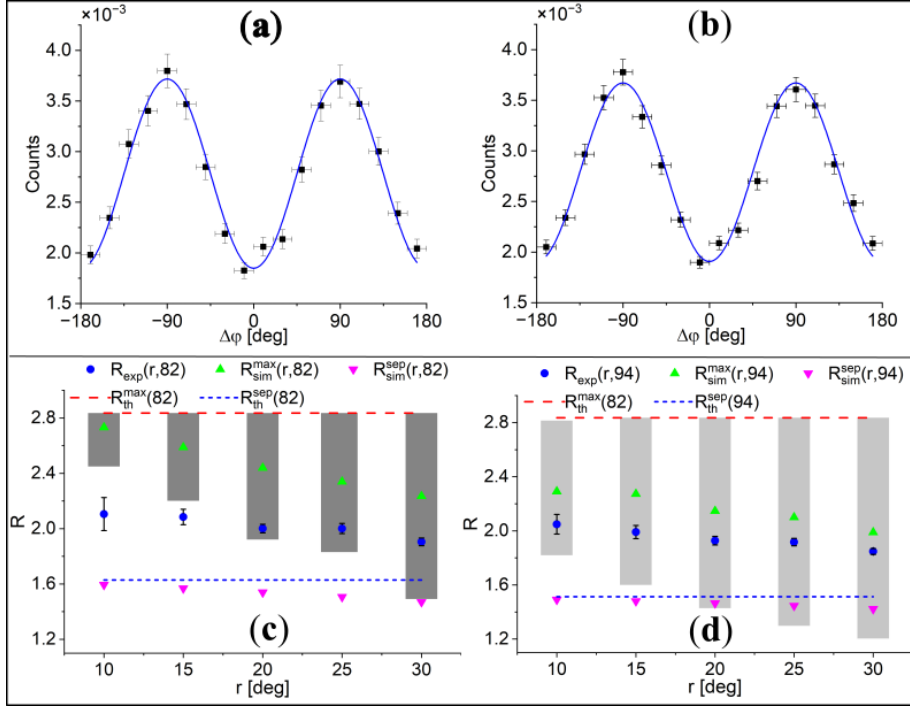


Fig. 3. **(a,b)** Experimental distributions of the $\Delta\varphi$ angle. Vertical bars denote statistical uncertainty, while horizontal bars indicate bin width. The left (a) and right (b) panels show results for events within a circle with the radius of 20° centered around $\theta_1 = \theta_2 = 82^\circ$, and $\theta_1 = \theta_2 = 94^\circ$, respectively. The solid curve represents the best fit of the function $A-B\cos(2\Delta\varphi)$, with A and B as free parameters. The details are described in the Methods section. **(c,d)** R values determined for events from different regions selected in the θ_1 vs θ_2 distributions. The left (c) and right (d) panels show results for events within circles with the radii of r , centered around $\theta_1 = \theta_2 = 82^\circ$, and $\theta_1 = \theta_2 = 94^\circ$, respectively (for the definition of circles see Fig. 6 in the Methods section). Experimental results are shown with blue points. Black bars denote the statistical uncertainty. The smaller the radius r , the fewer the number of events, and hence the larger the uncertainty. For comparison, the maximum possible value of R for the case when photons are maximally entangled ($R = 2.84$), achievable at $\theta_1 = \theta_2 = 82^\circ$, is indicated by the horizontal dashed-red line. The dashed-blue lines indicate the values of R in the case when the photons are not entangled for the scatterings at $\theta_1 = \theta_2 = 82^\circ$ ($R = 1.63$) and $\theta_1 = \theta_2 = 94^\circ$ ($R = 1.51$) in the left (c) and right (b) panels, respectively. Upward-pointing green triangles and downward-pointing magenta triangles demonstrate R values determined from the analysis of simulated data taking into account the geometry and characteristics of the J-PET scanner. The details of the simulations are described in the Methods section. Upward-pointing green triangles correspond to the result simulated assuming maximally entangled photons, while downward-pointing magenta triangles indicate results obtained assuming that the photons are separable. The shaded boxes show the range of theoretical R values, in a given selected circle, calculated for the case of maximally entangled photons.

DISCUSSIONS

This study demonstrates the first full-scale PET scanner capable of determining the polarization of annihilation photons by registering their Compton scatterings. The scanner is constructed from three cylindrical layers of plastic scintillator strips, in which annihilation photons interact almost exclusively through Compton interaction, compared to crystals where Compton effect constitutes e.g. 59% (BGO) or 69% (LYSO) [36, 39, 48, 49].

Therefore, plastic scintillators are the best suited for the quantum entanglement PET system. Another

TABLE I
 PARAMETER R_{exp} DETERMINED FOR THE RANGE OF SCATTERING ANGLES CENTERED AROUND 82° AND 94° WITH THE RADIUS $R = 20$ CM. THE VALUES ARE COMPARED TO THE ESTIMATIONS ASSUMING THAT PHOTONS ARE MAXIMALLY ENTANGLED (R_{sim}^{max}) AND SEPARABLE (R_{sim}^{sep}).

Range radius	Range centre	R_{exp}	R_{sim}^{max}	R_{sim}^{sep}
$r = 20^\circ$	$\theta_1 = \theta_2 = 82^\circ$	2.00 ± 0.03	2.44	1.54
$r = 20^\circ$	$\theta_1 = \theta_2 = 94^\circ$	1.93 ± 0.03	2.15	1.46

crucial characteristics of the scanner presented in this work is the large relative distance between subsequent Compton interactions in plastic scintillators. In the J-PET system it is equal on the average to 25 cm, compared to about 0.6 cm in BGO crystal scintillators.

This enables one to achieve with J-PET a high angular resolution of about 2° , and high purity of up to $\sim 95\%$ [24],

for the identification of first and second interactions, compared to only about 55% purity and about 6° angular resolution achieved in pixelated crystals [35, 50]. Moreover, in the presented J-PET system, the maximum efficiency for detecting double Compton interactions is within the angular range of $82^\circ \pm 30^\circ$, where the correlation is the highest (see Fig. 2d).

Using the data collected with the J-PET scanner we determined the distributions of the relative angle between the scattering planes of 511 keV photons ($\Delta\varphi$) originating from $e^+e^- \rightarrow 2\gamma$ annihilation in the porous polymer XAD4. The obtained shape of the $\Delta\varphi$ distributions exhibits $\cos(2\Delta\varphi)$ oscillations with a maximum at 90° , as expected for photons with perpendicular polarizations. The experimental $\Delta\varphi$ distributions were compared with predictions obtained under the assumptions that the photons are maximally entangled and that they are separable. The main observation reported in this work is that the correlations between the annihilation photons originating from the positron-electron annihilation in the porous polymer are larger than for the separable state but they are smaller than expected for the maximally entangled two-photon state. This finding is reported for the first time. Previous investigations of the $\Delta\varphi$ distribution for annihilation in metals, resulted in the R value consistent with the assumption that annihilation photons from the electron-positron annihilation are maximally entangled.[51, 52]

The most precise experiment so far, performed for photons from positron-electron annihilation in aluminium, yielded $R = 2.435 \pm 0.018$ [25], which taking into account the detector geometrical acceptance, is consistent with expectations for the maximally entangled two-photon state [25].

In metals, positrons annihilate only directly with electrons [10], whereas in the porous polymer XAD4, used in this study, positrons annihilate directly in only 32% of cases and in 68% of cases, the annihilation proceeds through the formation of positronium atoms [46]. In XAD4 material in 51% cases relatively long lived ortho-positronium atoms are formed. In XAD4 57% of oPs self-annihilate into 3-photons, while in 43% cases [46] positron from ortho-positronium annihilates by picking off electron from the surrounding molecules (see Fig. 1(a)). In this study the conversion of ortho-positronium on oxygen molecules is suppressed because air has been pumped out of the XAD4 material to 10^{-4} Pa using the dedicated

chamber and vacuum system [53].

We hypothesize that the non-maximal entanglement can be attributed to the annihilation of positrons with electrons bound to the molecules, when a positron from positronium annihilates with an electron from the surrounding atoms [18–20]. In general, when annihilation is from the mixed state the entanglement may be partially or fully lost [21, 54]. In the extreme scenario, assuming that the observed non-maximal value of R is due to the fact that in an α fraction of annihilation events the photons are maximally entangled and in $(1-\alpha)$ fraction of events the produced photons propagate independently of each other, we can estimate α as:

$$\alpha = \frac{R_{exp} - R_{sim}^{sep}}{R_{sim}^{max} - R_{sim}^{sep}}. \quad (6)$$

Based on the results obtained and reported in Table I, we estimate that the value of α is approximately 60%. This indicates that more than 40% of the annihilation photons originating in the XAD4 porous polymer are not maximally entangled.

To explore the origin of the observed non-maximal entanglement, dedicated experiments are required in which the annihilation mechanism can be identified, e.g., by additional measurements of the positron lifetime.

The annihilation of mixed states is expected in biological materials, which opens the possibility of applying R as a new diagnostic indicator that may be available in PET imaging [16, 54].

The imaging of polarization correlations requires coincident registration of four interactions, and therefore needs high-sensitivity scanners capable of multi-photon registration. New-generation PET scanners covering the whole body provide high enough sensitivity [2, 55–57], yet for imaging of polarization correlation a multi-photon acquisition is required, that is not yet available in the current clinical PET systems. In the case of crystal PET systems, multi-pixel readout will also be necessary [33, 35, 50].

The first PET scanner for clinical imaging of the polarization correlations for patients is being constructed at the Jagiellonian University using the J-PET technology based on plastic scintillators [36]. J-PET enables multi-photon registration [58–60] and determination of photons polarization [24, 61]. The scheme of the total-body J-PET system is presented in Fig. 4(a). The superimposed arrows indicate possible events which can be registered and used for imaging. Black solid arrows indicate 2-photon annihilation used routinely in the state-of-the-art PET for metabolic rate diagnosis. Green arrows indicate events that enable newly developed positronium imaging [58, 62], requiring registration of annihilation photons (green solid arrows) and prompt gamma emitted by radionuclide (green dashed arrow) [63, 65]. Blue arrows indicate topology of the four-signal events that can be used for the imaging of polarization correlations and hence the entanglement witness R , referred to as entanglement imaging. Blue-solid arrows denote annihilation photons, and dashed arrows indicate scattered photons. The total-body J-PET sensitivity profile for the registration of four-signal events useful for entanglement imaging [66] (blue solid curve) is compared in Fig. 4(b) to the sensitivity of standard metabolic imaging (black dotted curve) and positronium imaging (green dashed curve). The values of sensitivity were determined using Monte-Carlo simulations that take

into account the geometry and material composition of the scanner as described in detail in the Methods section. The sensitivity for the entanglement imaging is by order of magnitude smaller than the sensitivity for the standard 2γ metabolic imaging, but is larger than the sensitivity for positronium imaging. For the future clinical studies it is important to stress that the total-body J-PET sensitivity for entanglement imaging of about (3 cps/kBq) is at the level of the standard 2γ PET imaging of the previous generation PET scanners as Biograph True Point (4.2 cps/kBq) [67], Siemens Biograph 40 (10.0 cps/kBq) [68], Philips Gemini TF (6.6 cps/kBq) [69] or GE Discovery PET/CT 690 (7.5 cps/kBq) [70] that are still in use in clinical practice.

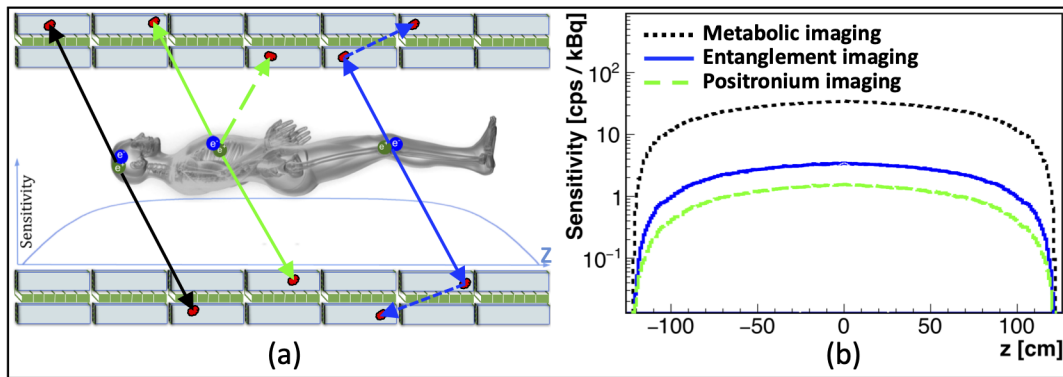


Fig. 4. **(a)** The axial cross section of the total-body J-PET being under construction at the Jagiellonian University. The designed scanner consists of 7 rings each built of two scintillator layers (blue) and one layer of wave-length shifter (green), described in detail in Ref. [36]. The long axial field of view of 250 cm will provide high 2γ registration sensitivity along the entire patient's body, as indicated by the blue curve [71]. The tomograph used in this work (shown in Fig. 2) constitutes a proof of concept prototype of the total-body J-PET. Superimposed arrows indicate three kinds of events enabling: (i) standard 2γ metabolic PET imaging based on the registration of two photons (black arrows) from the e^+e^- annihilation, as well as (ii) newly developed positronium imaging based on the registration of two annihilation photons (solid-green arrows) and the prompt gamma (dashed green arrow) [58, 62], and (iii) example event for the imaging of entanglement witness discussed in this work that include registration of annihilation photons (solid-blue arrows) and scattered photons (dashed-blue arrows) [23, 59, 66, 72]. **(b)** Registration sensitivities for different kind of events as a function of their origin along the axial position (z). The sensitivities for conventional 2γ metabolic imaging (dotted-black curve), entanglement imaging (solid-blue curve) and positronium imaging (dashed green curve) are shown. Details about the applied simulation method, detector geometry, and event selection criteria are described in the Methods section.

Summarizing, we developed and constructed the first PET system capable of imaging polarization correlations of annihilation photons. Using the data recorded with this scanner we demonstrated for the first time non-maximal entanglement of photons originating from positron annihilation in the porous polymer, contrary to the maximal entanglement observed for annihilations in aluminium and copper. The dependence of the degree of quantum correlation on the material opens perspective for application of entanglement imaging in medical diagnostics. We estimated that the total-body J-PET which is constructed from plastic scintillators will provide sufficient sensitivity for applying entanglement imaging in clinics.

METHODS

Positron annihilation chamber

In the reported experiment positrons were annihilating in the XAD-4 (CAS 37380-42-0) material [46]. Amberlite XAD-4 is a porous polymer resin with a high surface area and porous structure in which large fraction (68%) of positron annihilations proceed via positronium formation [46].

In the XAD-4 polymer, the two-photon annihilations proceed in about 31% via pick-off process of ortho-positronium, in 45% via direct e^+e^- annihilation and in about 24% via self annihilation of para-positronium [46]. Sodium ^{22}Na isotope with an activity of 1.1 MBq was employed as a positron emitter. The ^{22}Na source was sandwiched between two $7\mu\text{m}$ -thick kapton foils and enclosed on both sides by a few-mm-thick layer of the XAD4 porous polymer. The polymer and the positron source were situated within a dedicated chamber connected to a vacuum system that enabled the evacuation of air from the polymer pores to a pressure of 10^{-4} Pa [53]. The chamber was placed at the center of the J-PET scanner as illustrated in Fig. 2(b). The chamber was constructed from 1 mm thick polyamide 6 (PA6) with a density of 1.14 g/cm^3 , resulting in a negligible absorption (less than 1%)

of 511 keV photons [53].

J-PET scanner

J-PET is the first PET tomograph composed of plastic scintillators in which the Compton interaction is the main photon registration process [36–43]. The scanner used in this work consists of 192 plastic scintillators (EJ-230, $50 \times 1.9 \times 0.7\text{ cm}^3$) forming 3 concentric cylindrical layers (see Fig. 2(a)) [40]. The scintillators are connected at the ends to the vacuum tube photomultipliers (Hamamatsu R9800). The time and position of the interaction of photons (referred to as hits) along the scintillators are estimated by measuring the time of light signal arrivals to the photomultipliers [38]. The signals from the photomultipliers are sampled at four fixed thresholds (in mV: 30, 80, 190, 300) using Time to Digital Converters (TDCs) implemented in Field Programmable Gate Arrays (FPGA) devices [47]. The time stamps of the signals were recorded in the triggerless mode using the dedicated data acquisition system, which can process data streams at a speed of about 8 Gbps [60].

The calibration procedure and intra-synchronization of the timing signals between 192 detection modules are explained in previous work [73]. The hit-time and hit-position resolutions are equal to 250 ps and 25 mm, respectively [40]. The angular resolution for determining the scattering angle of annihilation photon amounts to 2.5° [24].

Events selection and classification

The collected data were analyzed using a dedicated framework developed based on C++ and Root (a data analysis tool developed at CERN [74, 75]) with detector-specific and advanced features [76]. Events useful for the study of the polarization correlations comprise four hits within 20 ns time window, 2 hits

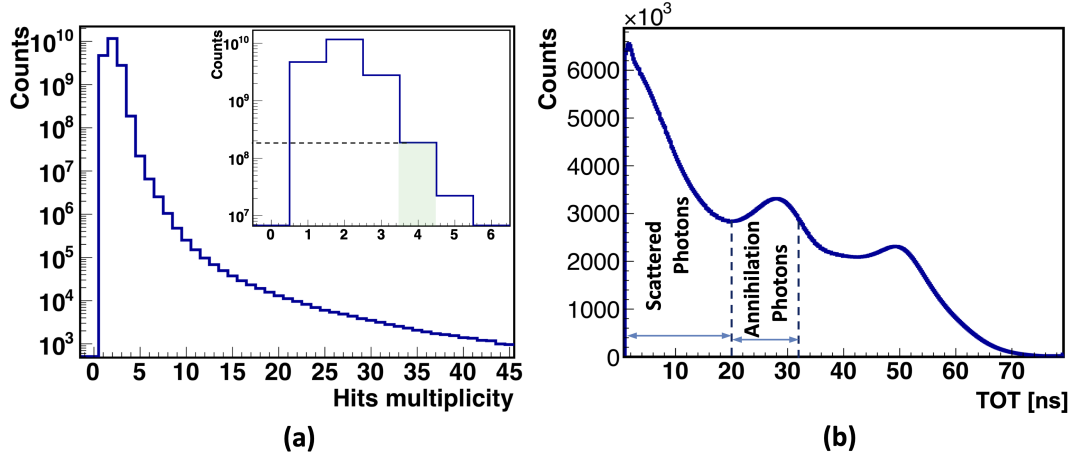


Fig. 5. (a) Distribution of hit multiplicity in events. Inset highlights 4-hit events used for the analysis in this work. The number of events with multiplicity of 1 is suppressed by prescaling the data with single hits in the analysis. (b) Time-over-threshold (TOT) histogram for all hits. Slopes at TOT values of about 32 ns and 56 ns correspond to the Compton edges resulting in maximum energy deposition by 511 keV annihilation photons, and 1275 keV prompt gamma (from ^{22}Na decay), respectively. Dashed vertical lines indicate the range of TOT values used to select candidates for annihilation photons (20 - 32 ns), and scattered photons (1 - 20 ns).

caused by primary photons (511 keV) and the remaining 2 hits caused by the corresponding scattered photons with lower energy (e.g. 275 keV for the scattering at 82°).

An example of such event is shown in Fig. 2(a) and Fig. 2(c).

Fig. 5(a) shows the histogram of the hit multiplicity in the event. For the analysis only events with multiplicity equal to 4 were accepted.

In the next step of analysis, as a first criterion to disentangle between the annihilation and scattered photons, the TOT value was used which is a measure of the energy deposition [42, 77]. For the 511 keV annihilation photons the energy depositions varies between 0 and 341 keV, and for the scattered photons of interest e.g. for the photons scattered at angles in the range of $82^\circ \pm 20^\circ$ the maximum energy deposition is equal to 218 keV and 98 keV for photons scattered under 52° and 112° , respectively.

Fig. 5(b) shows the distribution of TOT with superimposed vertical lines indicating ranges chosen for selecting scattered photons candidates ($1 \text{ ns} < \text{TOT} < 20 \text{ ns}$) and annihilation photons candidates ($20 \text{ ns} < \text{TOT} < 32 \text{ ns}$). The values of TOT are uniquely correlated with the energy deposition [77] and, for example, $\text{TOT} = 32 \text{ ns}$ corresponds to 341 keV (Compton edge for 511 keV photons), and $\text{TOT} = 56 \text{ ns}$ corresponds to 1062 keV (Compton edge for 1275 keV gamma from ^{22}Na decay [78]). Furthermore, for the annihilation photon candidates, the stringent back-to-back ($175^\circ < \theta < 185^\circ$) emission criterion was applied. Moreover, to ensure that photons are emitted from the source, an information from the tomographic image (Fig. 2(d)) was used. The image shows the density of annihilation points reconstructed based on the times and positions of hits identified as originating from annihilation photons. For further analysis, only events were considered for which the distance between the reconstructed annihilation site and the

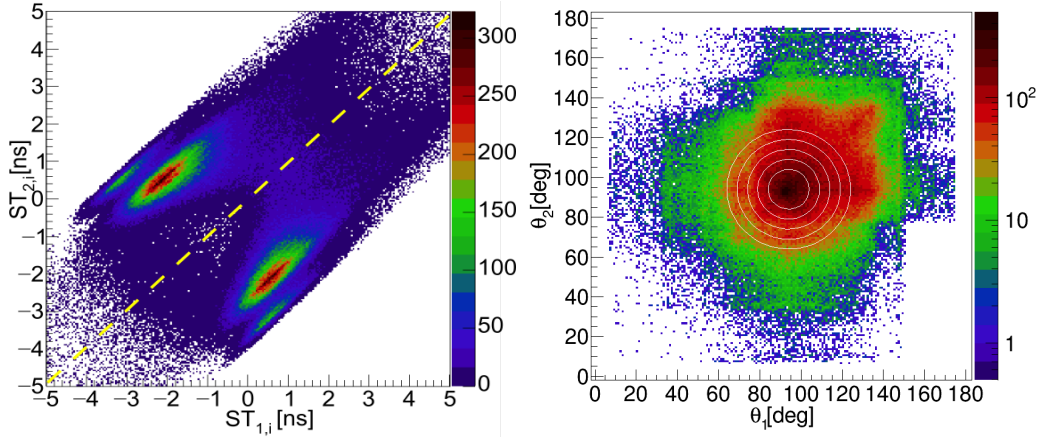


Fig. 6. (a) Distribution of ST_{2i} vs. ST_{1i} used to assign i^{th} scattered photon to the 1^{st} or 2^{nd} annihilation photon. Diagonal dashed-yellow line is used as a criterion for the selection. If the (ST_{1i}, ST_{2i}) point is below the diagonal then it is assumed that the i^{th} photon is a result of the scattering of the 1^{st} annihilation photon. Contrary, if the (ST_{1i}, ST_{2i}) point is above the diagonal then i^{th} scattered photon is assigned to the 2^{nd} annihilation photon. The observed split structure is due to the arrangement of the scintillators (Fig. 2). (b) Experimental distribution of the θ_2 vs. θ_1 angles. Due to the geometrical arrangement of scintillators in the J-PET scanner (Fig. 2), the maximum density of the (θ_2, θ_1) distribution is for the scatterings around the angles of $\theta_1 = \theta_2 = 94^\circ$. The white circles indicate regions with the radii of r of 10° , 15° , 20° , 25° and 30° used in the analysis (see Fig. 3).

center of the image (position of the source) was less than 1 cm in the x-y plane and less than 4 cm in the z direction. After selecting the hits in the event corresponding to the annihilation photons, as a next step the hits due to the scattered photons are assigned to the proper annihilation photon. By assigning indices 1 and 2 to the hits from annihilation photons and indices 3 and 4 to the hits from scattered photons, the next step in the analysis can be defined as testing two hypotheses: (i) the third photon is a result of scattering from the first annihilation photon and the fourth photon is a result of scattering from the second annihilation photon, and (ii) the third photon is a result of scattering from the second annihilation photon and the fourth photon is a result of scattering from the first annihilation photon. To test the hypothesis stating that i^{th} photon is a scatter of the j^{th} photon, we define a "Scatter Test" value: $ST_{j,i} = \Delta t_{j,i} - r_{j,i}/c$, where $\Delta t_{j,i} = t_j^{annihilation} - t_i^{scatter}$ and $r_{i,j}$ is the distance between the hit positions of the annihilation photon (r_j) and scatter photon (r_i). ST is a difference between the measured time of flight of the scattered photon, and the time of flight calculated for the light to travel between the i^{th} and j^{th} hits. In the case of ideal time and position resolution of the scanner, if the i^{th} photon is a scatter of the j^{th} photon than ST must be equal to zero. Fig. 6(a) shows the distribution of values $ST_{1,i}$ vs. $ST_{2,i}$ for testing the hypotheses whether the i^{th} scatter photon originates from 1^{st} or 2^{nd} annihilation photon. If the point $(ST_{2,i}, ST_{1,i})$ on the plot is below the diagonal then the i^{th} scatter photon is assigned to the 1^{st} annihilation photon. If it is above the diagonal, then it is assigned to the 2^{nd} annihilation photon. For the final analysis, only these events were selected for which each of the two different scattered photons was assigned to a different annihilation photon.

After the above-described event selection, including identification of annihilation photons and assignment of scattered photons, for each event the values of scattering angles θ_1 and θ_2 , and the relative angle between the scattering planes ($\Delta\varphi$) are determined. Fig. 6(b) shows the distribution of scatterings angle θ_2 versus θ_1 . The maximum density of registered events is observed for $\theta_2 = \theta_1 = 94^\circ$. This is due to the geometrical arrangement of scintillators in the J-PET scanner, as can be seen in Fig.2(a) and Fig.2(c). The white circles superimposed on the experimental distribution in Fig. 6(b) illustrate angular regions centered at $\theta_2 = \theta_1 = 94^\circ$ for which the $\Delta\varphi$ distributions and R parameter were determined and presented in Fig. 3(d).

Estimation of J-PET scanner acceptance and registration efficiency

The correction of the measured distributions for the geometrical acceptance and registration efficiency of the J-PET scanner is one of the most crucial steps in determining the polarization correlation of annihilation photons. Efficiency and acceptance were simultaneously determined in this work, and for the sake of brevity, we will refer to this combined quantity as 'efficiency' throughout the manuscript. Thus, in the following we will understand by efficiency the combined geometric acceptance, detection efficiency and event selection efficiency. Such defined efficiency was estimated as a function of the $\Delta\varphi$ angle using the GEANT4 simulation package [79, 80]. For this purpose, the full scanner geometry and material composition [40] were defined in the GEANT4 structure and the e^+e^- annihilations were simulated in the center of the detector assuming the fraction of direct annihilations, pPs and oPs formations, as it is known for the XAD4 porous polymer [46]. The method of simulations with the J-PET scanner was validated in the previous works, as described e.g. in Ref. [24, 42, 43, 59].

The response of the scanner was simulated. Next the simulated data were analysed using the same criteria as applied to the experimental data. Then, such determined $\Delta\varphi$ distributions were normalized to the original $\Delta\varphi$ distributions determined by simulating the annihilation photons interactions in the scanner and taking for the calculations a true scatterings angles [24]. The resulting normalized $\Delta\varphi$ spectra were used to correct the experimental $\Delta\varphi$ spectra for efficiency. Example of corrected $\Delta\varphi$ spectra are shown in Fig. 3(c) and Fig. 3(d).

Simulations of $\Delta\varphi$ distributions for separable and entangled annihilation photons

For simulations performed in this work it was assumed that the polarizations of the back-to-back propagating annihilation photons are perpendicular to each other. For the separable state interaction of each photon was simulated independently using GEANT4 package, in which the Compton scattering is simulated according to the Klein-Nishina formula [22]. In order to simulate the distribution for entangled photons we used the data simulated for separable state and preselected events such that the resulting distributions are as expected for the entangled photons. The method used for simulations of separable and quantum entangled photons was described in detail, and validated in Ref. [24].

Simulation of sensitivity for entanglement imaging with total-body J-PET scanner

Fig. 4(a) shows the scheme of the total-body J-PET scanner, which is currently under development at the Jagiellonian University. It consists of 168 detection modules arranged in 7 cylindrical rings spaced 2 cm apart and providing an extended axial field of view of 243 cm. Each module is constructed of an array of wavelength shifting strips (WLS) sandwiched between two layers of plastic scintillators. Each layer consists of 16 plastic scintillators (EJ-230) measuring $330 \times 30 \times 6 \text{ mm}^3$, while the middle layer is composed of 50 WLS with the dimensions of $108 \times 6 \times 3 \text{ mm}^3$ each, positioned perpendicular to plastic layers. The sensitivities of the total-body J-PET for the registration of different events of interest are estimated as a function of their axial origin ($x=y=0$), using the simulation package Geant4 Application for Tomographic Emission (GATE_V9) [81]. For the interaction cross-section of photons inside the scintillators, the `emlivermore_polar` was used as the physics model [79]. A linear source was axially aligned in the center of the total-body J-PET. For metabolic and entanglement imaging electron-positron annihilations into two 511 keV photons were simulated. While, for the positronium imaging an additional (isotropically emitted and not correlated with the annihilation photons) prompt gamma quantum with energy of 1160 keV was simulated. The 1160 keV correspond to the energy of prompt gamma from the ^{44}Sc isotope proposed for positronium imaging [71, 78]. In the calculations, only these annihilation photons were taken into account for which the energy deposition in the scintillator was in the range from 200 keV to 350 keV. For the prompt gamma an energy deposition larger than 350 keV was required. In the case of entanglement imaging, an energy larger than 30 keV was required.

ACKNOWLEDGEMENTS

The authors would like to thank Professor Steven Bass for helpful discussions. We also acknowledge the support provided by the Foundation for Polish Science through the TEAM POIR.04.04.00-00-4204/17 Program (P.M.); the National Science Centre of Poland through grants no. 2019/35/B/ST2/03562 (P.M.), 2021/42/A/ST2/00423 (P.M.), 2021/43/B/ST2/02150 (P.M.), 2022/47/I/NZ7/03112 (E.L.S.), 2020/38/E/ST2/00112 (E.P.d.R.), 2022/06/X/ST2/01444 (S.S.); the Ministry of Education and Science through grants no. SPUB/SP/490528/2021 (P.M.), IAL/SP/596235/2023 (P.M.); as well as the SciMat and qLife Priority Research Area budgets under the programme Excellence Initiative - Research University at the Jagiellonian University (P.M. and E.L.S.).

AUTHOR CONTRIBUTIONS

The experiment was conducted using the Jagiellonian Positron Emission Tomograph (J-PET). The J-PET scanner, the techniques of the experiment and this study was conceived by P.M. The data analysis was conducted by D.K. Signal selection criteria were developed by P.M. and S.S., applied by D. K., and verified by S.S. Authors: P.M., D.K., S.S., E.Y.B., S.C., N.C., A.C., C.C., E.C., M.D., K.D., M.G., B.J., K. Kacprzak, T. Kaplanoglu, Ł.K., K. Klimaszewski, T. Kozik, E.L., F.L., W.M., S.N., S.P., E.P.d.R., L.R., M.R., R.Y.S., M.S., E.L.S., P.T., K.T.A., K.V.E., and W.W. participated in the construction, commissioning, and operation

of the experimental setup, as well as in the data-taking campaign and data interpretation. N.C. under the supervision of S.N. and P.M. monitored the whole data taking campaign. M.G. and B.J. designed and constructed the positronium production chamber. S.N. optimized the working parameters of the detector. K.D. and K. Kacprzak, took part in developing the J-PET analysis and simulation framework. K.D., M.S., K.K. and E.P. del Rio performed timing calibration of the detector. K. Klimaszewski, W.W., L.R., and R.Y.S. managed the computing resources for high-level analysis and simulations. E.C. developed and operated short- and long-term data archiving systems and the computer center of J-PET. S.S. established relation between energy loss and TOT and dependence of detection efficiency on energy deposition. S.P. performed simulations for sensitivity profiles of metabolic, entanglement and positronium imaging. P.M. managed the whole project and secured the main financing. E.Ł.S contributed to securing financing of the project. The results were interpreted by P.M., S.S. and D.K. The manuscript was prepared by P.M., S.S., and D.K. and was then edited and approved by all authors.

DATA AVAILABILITY

The data sets collected in the experiment and analysed during the current study are available under restricted access due to the large data volume. Direct access to the data can be arranged on a reasonable request by contacting the corresponding authors.

COMPETING INTERESTS

The authors declare no competing interests.

REFERENCES

- [1] Alavi, A., Werner, T. J., Stepien, E. Ł. & Moskal, P. Unparalleled and revolutionary impact of PET imaging on research and day to day practice of medicine. *Bio-Algorithms and Med-Systems* **17**, 203–212 (2021).
- [2] Vandenberghe, S., Moskal, P. & Karp, J. S. State of the art in total body PET. *EJNMMI Phys.* **7**, 35 (2020).
- [3] Pither, R. PET and the role of in vivo molecular imaging in personalized medicine. *Expert Review of Molecular Diagnostics* **3**, 703–713 (2003).
- [4] Schulthess, G. K. Von., Steinert, H. C. & Hany, T. F. Integrated PET/CT: Current Applications and Future Directions. *Radiology* **238**, 405–422 (2006).
- [5] James, M. L. & Gambhir, S. S. A Molecular Imaging Primer: Modalities, Imaging Agents, and Applications. *Physiol. Rev.* **92**, 897–965 (2012).
- [6] McNamara, A.L., et al. Towards optimal imaging with PET: an in silico feasibility study. *Phys. Med. Biol.* **59**, 7587 (2014).
- [7] Toghyani, M., et al. Polarisation-based coincidence event discrimination: an in silico study towards a feasible scheme for Compton-PET. *Phys. Med. Biol.* **61**, 5803 (2016).

- [8] Romanchek, G., Shoop, G. and Abbaszadeh, S. Application of quantum entanglement induced polarization for dual-positron and prompt gamma imaging. *Bio Algorithms and Med Systems* **13**, 9–16 (2023).
- [9] Moskal, P., Jasińska, B., Stępień, E. Ł. & Bass, S. D. Positronium in medicine and biology. *Nature Reviews Physics* **1**, 527–529 (2019).
- [10] Bass, S.D., Mariazzi, S., Moskal, P. & Stępień, E. Positronium physics and biomedical applications. *Review of Modern Physics* **95**, 021002 (2023).
- [11] Harpen, M. D. Positronium: review of symmetry, conserved quantities and decay for the radiological physicist. *Med. Phys.* **31**, 57–61 (2004).
- [12] Jasińska, B. et al. Human tissues investigations using PALS technique. *Acta Phys. Polon. B* **48**, 1737–1747 (2017).
- [13] Moskal, P. et al. Performance assessment of the 2γ positronium imaging with the total-body PET scanners. *EJNMMI-Physics* **7**, 44 (2020).
- [14] Cassidy, D. B., Experimental progress in positronium laser physics. *Eur. Phys. J. D.* **72**, 53 (2018).
- [15] Acin, A., Latorre, J. I. & Pascual, P., Three-party entanglement from positronium. *Phys. Rev. A* **63**, 042107 (2001).
- [16] Hiesmayr, B. C. & Moskal, P. Witnessing Entanglement In Compton Scattering Processes Via Mutually Unbiased Bases. *Scientific reports* **9**, 8166 (2019).
- [17] Nowakowski, M. & Fierro, D.B. Three-photon entanglement from ortho-positronium revisited. *Acta Phys. Polon. B* **48**, 1955 (2017).
- [18] Coffman, V., Kundu, J. & Wootters, W. K. Distributed entanglement. *Phys. Rev. A* **61**, 052306 (2000).
- [19] Koashi, M. & Winter, A. Monogamy of quantum entanglement and other correlations. *Phys. Rev. A* **69**, 022309 (2004).
- [20] Horodecki, R., Horodecki, P., Horodecki, M. & Horodecki, K. Quantum entanglement. *Review of Modern Physics* **81**, 865-942 (2009).
- [21] Caradonna, P., D’Amico I., Jenkins D. G. & Watts D. P. Stokes-parameter representation for Compton scattering of entangled and classically correlated two-photon systems. *Phys. Rev. A* **109**, 033719 (2024).
- [22] Klein, O. & Nishina, T. über die Streuung von Strahlung durch freie Elektronen nach der neuen relativistischen Quantendynamik von Dirac.. *Zeitschrift für Physik* **52**, 853–868 (1929).
- [23] Moskal, P. et al. Potential of the J-PET detector for studies of discrete symmetries in decays of positronium atom - a purely leptonic system. *Acta Phys. Polon. B* **47**, 509–535 (2016).
- [24] Moskal, P. et al. Feasibility studies of the polarization of photons beyond the optical wavelength regime with the J-PET detector. *Eur. Phys. J. C* **78**, 970 (2018).
- [25] Ivashkin, A. et al. Testing entanglement of annihilation photons. *Scientific reports* **13**, 7559 (2023).
- [26] Knights, P., Ryburn, F., Tungate, G. & Nikolopoulos, K. Studying the effect of polarization in

- Compton scattering in the undergraduate laboratory. *Eur. J. Phys.* **39**, 025203 (2018).
- [27] Pryce, M. L. H. & Ward, J. C. Angular Correlation Effects with Annihilation Radiation. *Nature* **160**, 435 (1947).
- [28] Snyder, H. S., Pasternack, S. & Hornbostel, J. Angular Correlation of Scattered Annihilation Radiation. *Phys. Rev.* **73**, 440–448 (1948).
- [29] Hanna, R. C. Polarization of Annihilation Radiation. *Nature* **162**, 332 (1948).
- [30] Wu, C. S. & Shaknov, I. The Angular Correlation of Scattered Annihilation Radiation. *Phys. Rev.* **77**, 136 (1950).
- [31] Langhoff, H. Die Linearpolarization der Vernichtungsstrahlung von Positronen. *Zeitschrift für Physik* **160**, 186–193 (1960).
- [32] Kasday, L. R., Uliman, J. D. & Wu, C. S. Angular correlation of Compton-scattered annihilation photons and hidden variables. *Nuov Cim B* **25**, 633–661 (1975).
- [33] Watts, D. P. et al. Photon quantum entanglement in the MeV regime and its application in PET imaging. *Nature comm.* **12**, 2646 (2021).
- [34] Bohm, D. & Aharonov, Y. Discussion of Experimental Proof for the Paradox of Einstein, Rosen, and Podolsky. *Phys. Rev.* **108**, 1070–1076 (1957).
- [35] Parashari, S. et al. Optimization of detector modules for measuring gamma-ray polarization in Positron Emission Tomography. *Nuclear Instrum. Methods Phys. Res. A* **1040**, 167186 (2022).
- [36] Moskal, P. et al. Simulating NEMA characteristics of the modular total-body J-PET scanner—an economic total-body PET from plastic scintillators. *Phys. Med. Biol.* **66**, 175015 (2021).
- [37] Moskal, P. et al. Novel detector systems for the positron emission tomography. *Bio Algorithms and Med Systems* **7**, 73–78 (2011).
- [38] Moskal, P. et al. Test of a single module of the J-PET scanner based on plastic scintillators. *Nucl. Instrum. Meth.* **A764**, 317–321 (2014).
- [39] Moskal, P. et al. Time resolution of the plastic scintillator strips with matrix photomultiplier readout for J-PET tomograph. *Phys. Med. Biol.* **61**, 2025–2047 (2016).
- [40] Niedźwiecki, S. et al. J-PET: a new technology for the whole-body PET imaging. *Acta Phys. Polon.* **B48**, 1567 (2017).
- [41] Moskal, P. et al. Synchronization and Calibration of the 24-Modules J-PET Prototype With 300-mm Axial Field of View. **70**, 2000810 (2020).
- [42] Sharma, S. et al. Estimating relationship between the Time Over Threshold and energy loss by photons in plastic scintillators used in the J-PET scanner. *EJNMMI-Physics* **7**, 39 (2020).
- [43] Sharma, S. et al. Efficiency determination of J-PET: first plastic scintillators-based PET scanner. *EJNMMI-Physics* **10**, 28 (2023).
- [44] Jones, T. & Townsend, D. History and future technical innovation in positron emission tomography. *Journal of Medical Imaging* **4**, 011013 (2017).
- [45] Surti, S., Pantel, A. R. & Karp, J. S. Total Body PET: Why, How, What for?. *IEEE Trans. on*

- Radiation and Plasma Med. Sci.* **4**, 283–292 (2020).
- [46] Jasińska, B. et al. Determination of the 3γ fraction from positron annihilation in mesoporous materials for symmetry violation experiment with J-PET scanner. *Acta Phys. Polon. B* **47**, 453–460 (2016).
- [47] Pałka, M. et al. Multichannel FPGA based MVT system for high precision time (20 ps RMS) and charge measurement. *JINST* **12**, P08001 (2017).
- [48] NIST XCOM photon cross sections database, <https://www.nist.gov/pml/xcom-photon-cross-sections-database>.
- [49] Eijk, C.W.E. Van. Inorganic scintillators in medical imaging detectors. *Nuclear Instrum. Methods Phys. Res. A* **509**, 17–25 (2003).
- [50] Kozuljevic, A. M. et al. Study of Multi-Pixel Scintillator Detector Configurations for Measuring Polarized Gamma Radiation. *Condens. Matter* **6**, 43 (2021).
- [51] Parashari, S. et al. Closing the door on the “puzzle of decoherence” of annihilation quanta. *Physics Letters B* , 138628 (2024).
- [52] Bordes, J. et al. A first detailed study of the quantum decoherence of entangled gamma photons. *arXiv* , 2312.05045 [quant-ph] (2023).
- [53] Gorgol, M., Jasińska, B., Kosior, M., Stępień, E. & Moskal, P. Construction of the Vacuum Chambers for J-PET Experiments with Positron Annihilation. *Acta Phys. Polon. B* **51**, 293 (2020).
- [54] Hiesmayr, B. C. & Moskal, P. Genuine Multipartite Entanglement in the 3-Photon Decay of Positronium. *Scientific reports* **7**, 15349 (2017).
- [55] Spencer, B. A. et al. Performance Evaluation of the uEXPLORER Total-Body PET/CT Scanner Based on NEMA NU 2-2018 with Additional Tests to Characterize PET Scanners with a Long Axial Field of View. *J Nucl Med.* **62**, 861–870 (2021).
- [56] Prenosil, G.A. et al. Performance Characteristics of the Biograph Vision Quadra PET/CT System with a Long Axial Field of View Using the NEMA NU 2-2018 Standard. *J Nucl Med.* **63**, 476–484 (2022).
- [57] Dai, B. et al. Performance evaluation of the PennPET explorer with expanded axial coverage. *Phys. Med. Biol.* **68**, 095007 (2023).
- [58] Moskal, P. et al. Positronium imaging with the novel multiphoton PET scanner. *Science advances* **7**, 42, 1–9 (2021).
- [59] Moskal, P. et al. Testing CPT symmetry in ortho-positronium decays with positronium annihilation tomography. *Nature Communications* **12**, 5658 (2021).
- [60] Korcyl, G. et al. Evaluation of single-chip, real-time tomographic data processing on fpga soc devices. *IEEE Transactions on Medical Imaging* **37**, 2526–2535 (2018).
- [61] Moskal, P. et al. Discrete symmetries tested at 10^{-4} precision using linear polarization of photons from positronium annihilations. *Nat. Commun* **15**, 78 (2024).
- [62] Moskal, P. Positronium imaging. *Proceedings of the 2019 IEEE NSS and MIC Conference* , (2019).
- [63] Moskal, P. et al. Time resolution of the plastic scintillator strips with matrix photomultiplier readout

- for J-PET tomograph. *Phys. Med. Biol.* **61**, 2025–2047 (2016).
- [64] Moskal, P. et al. Feasibility study of the positronium imaging with the J-PET tomograph. *Phys. Med. Biol.* **64**, 055017 (2019).
- [65] Moskal, P. et al. Performance assessment of the 2gamma positronium imaging with the total-body PET scanners. *EJNMMI-Physics* **7**, 44 (2020).
- [66] Moskal, P. Towards total-body modular PET for positronium and quantum entanglement imaging. *Proceedings of the 2018 IEEE Nuclear Science Symposium and Medical Imaging Conference (NSS/MIC)*, (2018).
- [67] Carlier, T. et al. ^{90}Y -PET imaging: Exploring limitations and accuracy under conditions of low counts and high random fraction. *Med. Phys.* **42**, 4295 (2015).
- [68] Carlberg, A. M. et al., Quantitative comparison of PET performance—Siemens Biograph mCT and mMR. *EJNMMI Phys.* **3**, 5 (2016).
- [69] Surti, S. et al. Performance of Philips Gemini TF PET/CT Scanner with Special Consideration for Its Time-of-Flight Imaging Capabilities. *J Nucl Med.* **48**, 471–480 (2007).
- [70] Bettinardi, V. et al. Physical Performance of the new hybrid PET/CT Discovery-690. *Med. Phys.* **38**, 5394–5411 (2011).
- [71] Moskal, P. & Stepien, E.L. Prospects and clinical perspectives of Total-Body PET imaging using plastic scintillators. *PET Clin.* **15**, 439-452 (2020).
- [72] Moskal, P. Positronium and Quantum Entanglement Imaging: A New Trend in Positron Emission Tomography. *Proceedings of the 2021 IEEE Nuclear Science Symposium and Medical Imaging Conference (NSS/MIC)*, (2021).
- [73] Dulski, K., Silarski, M. & Moskal, P. A method for time calibration of PET systems using fixed β^+ radioactive source. *Acta Phys. Polon. B* **51**, 195–200 (2020).
- [74] Brun, R. & Rademakers, F. ROOT - An object oriented data analysis framework. *Nucl. Instrum. Meth.* **389**, 81–86 (1997).
- [75] Rademakers, F. et al., Root-project/root:v6.16/02. *Acta Phys. Polon. B*, (2018).
- [76] Krzemien, W. et al. J-PET Framework: Software platform for PET tomography data reconstruction and analysis. *Software X* **11**, 100487 (2020).
- [77] Sharma, S. TOT Method for the Disentanglement of Photons in Positron Annihilation Lifetime Spectroscopy. *Acta Phys. Pol. A* **137**, **2**, 1-4 (2020).
- [78] Das, M. et al. Estimating the efficiency and purity for detecting annihilation and prompt photons for positronium imaging with J-PET using toy Monte Carlo simulation. *Bio-Algorithms and Med-Systems* **19**, 87–95 (2023).
- [79] Agostinelli, S. et al. Geant4—a simulation toolkit. *Nucl. Instrum. Meth.* **506**, 250–303 (2003).
- [80] Allison, J. et al. Recent developments in Geant4. *Nucl. Instrum. Meth.* **835**, 186–225 (2016).
- [81] Sarrut, D. et al. Advanced Monte Carlo simulations of emission tomography imaging systems with GATE. *Phys. Med. Biol.* **66**, 10TR03 (2021).